

Lithium-ion dynamics in synthetic quartz studied via the NMR of implanted $^8\text{Li}^+$

W. Andrew MacFarlane,^{1,2,3,*} Ryan M. L. McFadden,^{1,2,†} Signy Spencer,^{1,2} Aris Chatzichristos,^{2,4,‡} John O. Ticknor,^{1,2} David L. Cortie,^{2,§} Martin H. Dehn,^{2,4,¶} Sarah R. Dunsiger,³ Derek Fujimoto,^{2,4,†} Z. H. Jang,⁵ Victoria L. Karner,^{1,2,†} Robert F. Kiefl,^{4,2,3} Gerald D. Morris,³ and Monika Stachura^{3,6}

¹Department of Chemistry, University of British Columbia, Vancouver, BC V6T 1Z1, Canada

²Stewart Blusson Quantum Matter Institute, University of British Columbia, Vancouver, BC V6T 1Z4, Canada

³TRIUMF, Vancouver, BC V6T 2A3, Canada

⁴Department of Physics, University of British Columbia, Vancouver, BC V6T 1Z1, Canada

⁵Department of Physics, Kookmin University, 77 Jeongneung-ro, Seongbuk-gu, Seoul, 02707, Korea

⁶Department of Chemistry, Simon Fraser University, Burnaby, BC V5A 1S6, Canada

(Dated: March 26, 2025)

We report β -detected nuclear magnetic resonance (β -NMR) measurements of implanted $^8\text{Li}^+$ in a synthetic single crystal of α - SiO_2 (quartz). At 6.55 Tesla, the spectrum is comprised of a large amplitude broad resonance and a quadrupolar multiplet that is only revealed by an RF comb excitation. The quadrupole splitting is surprisingly small, increases with temperature, and provides information on the implantation site. Supercell density functional theory calculations show that the small EFG is consistent with an in-channel interstitial site (Wyckoff $3a$). The spin-lattice relaxation is unexpectedly fast and strongly temperature dependent with a diffusive peak above 200 K and a second more prominent relaxation peak at lower temperature. Analysis of the diffusive relaxation yields an activation barrier 178(43) meV for the isolated Li^+ in the range of other measurements and calculations. To account for many of the other features of the data, it is suggested that some of the implanted ions trap an electron forming the neutral Li^0 , which is stable over a narrow range of temperatures.

I. INTRODUCTION

Crystalline quartz (SiO_2) in its low temperature α -polytype is a wide band gap oxide insulator useful for its piezoelectric, optical and robust high temperature properties. Its chemical

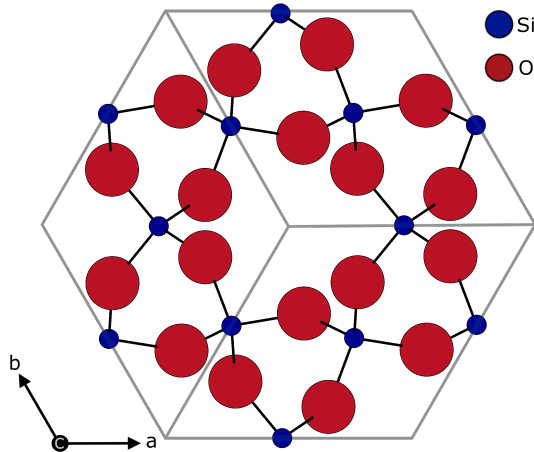


Figure 1. Projection of the structure along the c -axis showing the large open channel centered on the c edge of the conventional unit cell shown in Appendix C.

simplicity conceals significant complexity in its crystal structure composed of chains of corner sharing SiO_4 tetrahedra winding along the c -axis to form a chiral crystal (space group $P3_121$ or $P3_221$ depending on the handedness[1]) as demonstrated, for example, by its optical rotatory power[2]. The linked chains of tetrahedra surround open channels as illustrated by the c -axis projection shown in Figure 1. These channels admit highly one-dimensional (1D) mobility of small interstitial ions such as Li^+ , and this forms the motivation for the experiments reported here, where we use nuclear magnetic resonance (NMR) to study the short-lived radioisotope $^8\text{Li}^+$ implanted into high purity synthetic quartz. Previously, we had found very interesting dynamic properties of implanted $^8\text{Li}^+$ in another 1D Li^+ conductor, rutile TiO_2 [3, 4], and we were interested to see if this was more general. Even though the macroscopic Li^+ conductivity of quartz is quite low[5, 6], there are solid state battery designs featuring SiO_2 in the solid electrolyte interphase (SEI) layer at a Si electrode[7–10]. The properties of interstitial alkalis are also of geological interest in various forms of natural quartz[11, 12]. Even in synthetic crystals[13], they are known to contribute to dielectric loss[14, 15] limiting the performance of some piezoelectric devices and motivating development of electrochemical sweeping methods[16].

Dimensional confinement significantly modifies diffusive dynamics[17]. The most extreme case that still allows long range transport is when the motion is confined to 1D, which is relevant for many real-world systems (e.g., ion channels that traverse the cell membrane, water in nanoporous media like carbon nanotubes[18] or microfluidic devices, and atomic diffusion in certain crystal matrices where the structure naturally provides 1D channels such as α - SiO_2). A distinguishing feature of 1D diffusion is that the mean square displacement of a diffuser grows with time as \sqrt{t} rather than linearly, i.e. it is intrinsically “subdiffusive”[19–21]. The 1D character of the motion of Li^+ in quartz is demonstrated by its highly

* Email:wam@chem.ubc.ca

† Current address: TRIUMF, Vancouver, BC V6T 2A3, Canada

‡ Current address: Accenture, Athens 145 64, Greece

§ Current address: Australian Nuclear Science and Technology Organisation, Lucas Heights, New South Wales 2234, Australia

¶ Current address: D-Wave Systems, Burnaby, BC V5G 4M9, Canada

anisotropic conductivity which is several orders of magnitude larger parallel to the channels, with a temperature dependence governed by a relatively large energy barrier ($E_a \sim 1$ eV)[5, 6]. However, this E_a is not likely intrinsic. Rather, it probably represents the binding energy at dilute crystal defects that act as trap sites. For example, Al^{3+} (substitutional for Si^{4+}) has a relative charge of -1 which binds a small mobile interstitial cation (H^+ , Li^+ , Na^+) in the adjacent channel. Trapping at such charged defects is likely the rate limiting process for the macroscopic ionic conductivity. This is confirmed by radiation induced conductivity (RIC) measurements[22], where holes from electron-hole pair excitations can localize at an Al^{3+} impurity, neutralizing it and releasing the bound alkali[23]. There is good evidence that the resulting RIC is due to mobility of the liberated alkalis[24–26], and it shows a much smaller $E_a \sim 140$ meV, which is probably the intrinsic barrier[24]. Remarkably, the trapping effect of Al vanishes in the dense limit in the structurally related superionic conductor β -eucryptite LiSiAlO_4 [27]. That the liberated Li^+ becomes mobile above ~ 150 K is further demonstrated by the production of the neutral Li^0 by a two step (Xray) irradiation. The first step (which frees the Li^+ from an Al^{3+}) must be done above 150 K to allow the Li^+ to thermally diffuse some distance from the Al hole center [AlO_4]⁰[28]. The sample is then cooled to 77 K (freezing the now isolated interstitial Li^+) and a second irradiation step provides a radiolytic electron that is captured by the Li^+ to form the neutral.

Here, we use the NMR spin-lattice relaxation (SLR) rate $1/T_1$ to sense diffusive dynamics. This is the rate at which the initially polarized nuclear spin relaxes towards thermal equilibrium where the polarization is nearly zero. It is determined by fluctuations of the local electromagnetic field at the NMR frequency ω_0 that, for a diffusing species, reflect the stochastic site-to-site hopping. This quantity has been used extensively to study diffusion in solids at the microscopic scale[29–36]. Its primary feature is a maximum in $1/T_1(T)$ when the fluctuation rate (the elementary hop rate $1/\tau$) matches ω_0 , known as the Bloembergen-Purcell-Pound (BPP) peak[37]. Based on the RIC, we anticipate the BPP peak will be above ~ 150 K. The strong T dependence of the rate on either side of the BPP peak reflects the activated T dependence of the hop rate,

$$\frac{1}{\tau} = \frac{1}{\tau_0} e^{-\frac{E_a}{k_B T}}, \quad (1)$$

where E_a is the barrier to hopping, k_B is the Boltzmann constant, and $1/\tau_0$ is the exponential prefactor. In an elementary microscopic picture, $1/\tau_0$ represents a typical vibrational frequency on the order of 10^{12} Hz. The fluctuation spectral density for stochastic hopping depends on dimensionality [30, 35] resulting in a specific ω_0 and T dependence of $1/T_1$. However, experimentally in solids with very high ionic mobility, there are often deviations from this ideal behavior. For example, the prefactor extracted from $1/T_1(T)$ may differ by several orders of magnitude from its expected range. Such prefactor anomalies[29, 38] may be influenced by both dimensionality and disorder, though they remain poorly understood[39]. The anomalous prefactors we found in TiO_2 [3] suggested that we may be able to study this phenomenon more systematically by

implanting the same mobile $^8\text{Li}^+$ into a number of different 1D hosts in the ultra-dilute limit.

In α - SiO_2 , we find the spin-lattice relaxation for ^8Li is unexpectedly fast and strongly temperature dependent with a broad diffusive peak above 200 K (at high field) and a second more prominent relaxation peak at lower temperature. The diffusive relaxation yields an activation barrier for the isolated Li^+ in the range of other measurements and calculations. However, the range over which it is the dominant relaxation mechanism limits the ability to discern characteristic features of 1D diffusion. In high field, the spectrum has two components, a large amplitude broad resonance and a quadrupolar multiplet that is only revealed by an RF comb excitation[40]. The quadrupole splitting is surprisingly small and increases with temperature. Its value provides information on the implantation site. To account for many unexpected features of the data, it is suggested that a fraction of the implanted ion traps an electron forming the neutral $^8\text{Li}^0$.

The remainder of this paper is organized as follows: Section II describes the experiment; the results and their basic analysis is presented in Section III. Further analysis and interpretation are presented in Section IV with a summary in Section V. Complementary information peripheral to the main results, such as some additional data and calculation details, is given in Appendices A to E.

II. EXPERIMENT

The ion-implanted β -NMR experiments were conducted at TRIUMF’s Isotope Separator and Accelerator facility which provides low energy (1 – 30 keV) ion beams of short-lived radioisotopes for materials research. Here we use $^8\text{Li}^+$ with nuclear spin $I = 2$, a half-life of $\tau_{1/2} = 848$ ms, a gyromagnetic ratio $\gamma = 2\pi \times 6.3019$ MHz T^{-1} , and quadrupole moment of +32.6 mb [41, 42]. The beam is transported through a high vacuum beamline and polarized in-flight using a fast collinear optical pumping scheme using circularly polarized light. The direction of polarization (helicity) is selected by the handedness of the light polarization. In the measurement, helicity is alternated systematically with data collected and stored separately. At the end of the beamline, the $^8\text{Li}^+$ is directed into one of two NMR spectrometers where it is implanted into the sample in a differentially pumped vacuum space with a typical background pressure of 10^{-10} Torr. The spectrometer provides a static magnetic field B_0 along the spin polarization, as well as a transverse radiofrequency (RF) field. The NMR signal is detected via the parity violating weak β -decay which correlates the emission direction of the high energy β electron with the nuclear spin at the instant of decay. This is accomplished with two fast plastic scintillators (that detect the emitted β s with a high efficiency) located on opposite sides of the sample along the polarization direction z . For example, in the high field spectrometer, a static field in the range of several T is applied along the beam direction by a high homogeneity superconducting solenoid. The scintillation detectors are the “forward” (F) counter, downstream of the sample, and the upstream “backward” (B) counter with an aperture to allow the beam to pass through it. The

beta counts N_F and N_B in these detectors are measured under specific conditions, and the experimental asymmetry, defined by,

$$A(t) = \frac{N_F(t) - N_B(t)}{N_F(t) + N_B(t)} = \mathcal{A}_0 p_z, \quad (2)$$

where p_z is the polarization averaged over the ensemble of decaying spins (i.e., $p_z = \langle I_z \rangle / I$), is extracted. The amplitude \mathcal{A}_0 is determined by the intrinsic asymmetry of the beta decay (1/3 for ${}^8\text{Li}$), the effective detector solid angles at B_0 , and the performance of the optical polarizer.

Three types of measurements were performed: 1) SLR; 2) resonance, and 3) a quadrupolar resonance comb. In 1), the ${}^8\text{Li}^+$ beam is pulsed (4 s pulse) using an electrostatic kicker, followed by a (12 s) beam-off period. This cycle repeats, and the time-resolved β -decay counts are monitored with a time-resolution of 10 ms. Data from subsequent pulses are combined to obtain higher statistics, for a typical total run time of ~ 30 min. In 2), the ${}^8\text{Li}^+$ is continuously implanted while the single tone RF frequency is stepped slowly through a range of frequencies around the NMR frequency $\omega_0 = 2\pi\nu_0 = \gamma B_0$ using a frequency step that is a small fraction of the linewidth. At each step, the β counts are accumulated over a short integration period (1 s). The scan is then repeated, alternating both the polarization direction as well as the frequency sweep direction, to minimize systematics and increase statistics. The scans are then combined to yield the measured spectrum. When the RF frequency matches ν_0 , it causes rapid spin precession about the RF field, and the asymmetry is reduced. In 3), the RF is an equal amplitude comb, the sum of four equal amplitude sine waves at frequencies: $\tilde{\nu}_0 \pm \tilde{\nu}_q$ and $\tilde{\nu}_0 \pm 3\tilde{\nu}_q$. The fixed parameter $\tilde{\nu}_0$ is chosen as the center of the resonance from 2), and the comb splitting parameter $\tilde{\nu}_q$ is scanned over a defined range (alternating helicity and frequency step direction). For a resonance split into the $2I = 4$ quadrupolar satellites, the comb can simultaneously excite all the single quantum transitions when $\tilde{\nu}_q$ matches the quadrupole frequency ν_q , strongly enhancing (up to $\sim 10\times$) the signal amplitude[40]. This is particularly useful for well-defined quadrupolar lines from a specific crystallographic site that would be difficult or impossible to detect in the presence of other overlapping lines.

The data is taken on a hydrothermally grown commercial single crystal of α - SiO_2 (SurfaceNet, Rheine, Germany). The colorless transparent crystal measuring $8 \times 10 \times 0.5$ mm was oriented with its large flat face perpendicular to the c -axis which was “epi-polished” with a surface roughness ~ 1 nm. The Al content is on the order of 5 ppm or less, and the main impurity is hydrogen which can be as high as 0.25% relative to Si[13]. In Appendix A, we also include a comparison with an “N grade” fused quartz sample (Tosoh, Tokyo, Japan) at room temperature. In the course of these measurements, we also observed *scintillation* in quartz at low temperature consistent with its known ionoluminescence[43].

The primary data at $B_0 = 6.55 \text{ T} \parallel c$ uses an implantation energy of 25 keV, but we also include data from lower fields up to 22 mT $\perp c$ at 28 keV. SRIM[44] simulations predict a mean range of 163(181) nm with a straggle of 55(59) nm at 25(28) keV. However, the implantation direction is along c in both

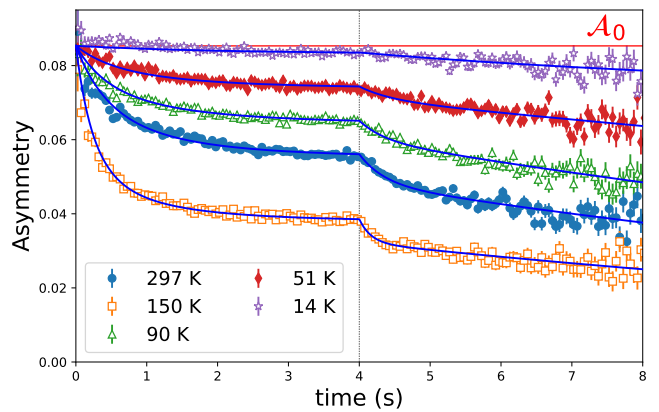


Figure 2. The experimental beta decay asymmetry as a function of time showing the temperature dependence of the spin-lattice relaxation of ${}^8\text{Li}^+$ implanted into quartz with $B_0 = 6.55 \text{ T} \parallel c$. The vertical line marks the end of the beam pulse. The relaxation is fastest at an intermediate temperature and shows a biexponential character (blue curves) with a fast relaxing fraction that evolves with temperature. The data are shown with 50 ms bins for clarity. Note the time dependence of the statistical error bars reflects the radioactive lifetime of ${}^8\text{Li}$.

cases, and in view of the structure shown in Figure 1, there is likely a channelled fraction that penetrates considerably further than the simulations predict. We also note that, compared to typical stable isotope ion beams, the radioactive ${}^8\text{Li}^+$ beam is very low intensity. The maximum beam rate was $\sim 5 \times 10^6$ ions per second in a beamspot about 2 mm in diameter (for a flux $\sim 2 \times 10^8$ ions/cm 2 /s). The total fluence over the course of the experiment was $\sim 5.5 \times 10^{12}$ ions/cm 2 .

III. RESULTS

A. Spin-Lattice Relaxation

Examples of the high magnetic field relaxation data are shown in Figure 2, exhibiting the bipartite relaxation (recovery curve) due to the 4 second beam pulse. At room temperature, the relaxation is remarkably fast for a nonmagnetic insulator. The relaxation is not directly related to the observed scintillation. For example, we find an even stronger scintillation in α - Al_2O_3 , but in contrast, the relaxation in high magnetic fields is very slow[45]. It is also strongly (and nonmonotonically) temperature dependent with the fastest relaxation in the vicinity of 150 K. The simplest relaxation function that can fit the data is a biexponential where the spin polarization at time t after implantation follows,

$$p_z(t) = (1 - f_f)e^{-\lambda_s t} + f_f e^{-\lambda_f t}, \quad (3)$$

with about a factor of 10 between the two SLR rates $\lambda_i \equiv (1/T_1)_i$. The data were fit to this function convoluted with the square beam pulse with a common T -independent initial asymmetry $\mathcal{A}_0 = 0.0885(1)$, consistent with the full asymmetry from calibration runs in MgO and ZnO. In this fit, the fraction f_f was a free parameter varying with temperature,

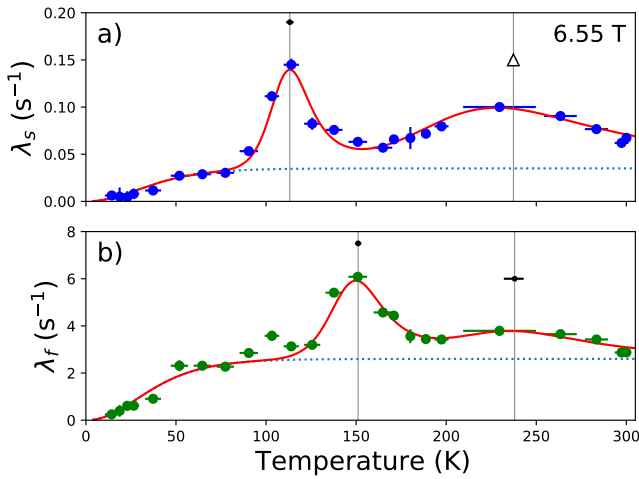


Figure 3. The a) slow and b) fast relaxation rates at 6.55 T as a function of temperature, showing a sharper low temperature and broader high temperature peak. From parabolic fits in the vicinity of the maxima, the peak temperatures are shown as the black symbols and vertical lines. The background rate (dotted line) slows below 50 K. The red curves are a guide to the eye.

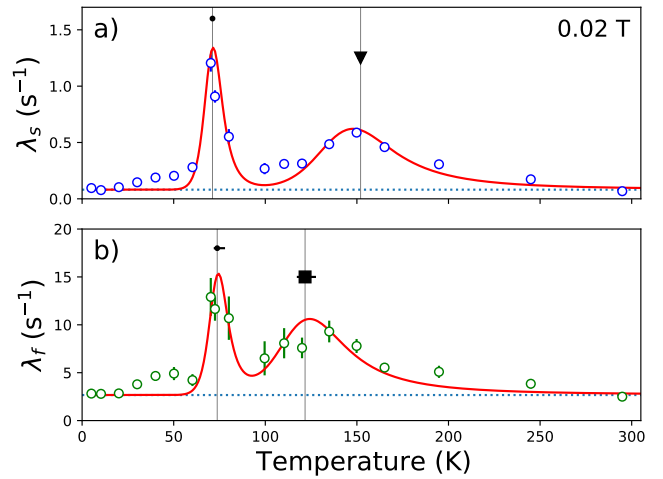


Figure 5. The a) slow and b) fast relaxation rates at 20 mT as a function of temperature exhibits features similar to high field. From parabolic fits, the peak temperatures are shown as the black symbols and vertical lines. The constant background rate is shown as the dotted line, and the red curves are a guide to the eye.

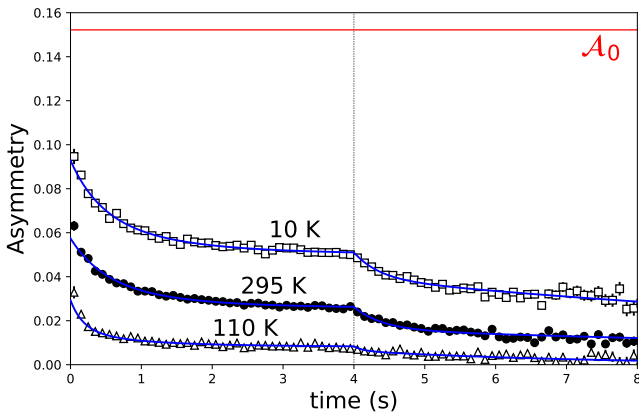


Figure 4. Spin-lattice relaxation of ${}^8\text{Li}$ at 20 mT $\perp c$. The red line indicates the calibrated full asymmetry \mathcal{A}_0 , clearly demonstrating a large missing fraction at all temperatures. The data are shown with 100 ms bins for clarity with biexponential fits.

see Figure 12a). The resulting global fit was good (reduced $\chi^2 = 1.03$), with some examples shown in Figure 2.

The relaxation rates λ_i from this fit are shown versus T in Figure 3. They reveal a low temperature increase to ~ 50 K (similar in both components) followed by sharp peaks at different temperatures in the slow (115 K) and fast (151 K) components and much broader peaks around 250 K in both. To locate the peak positions, subsets of the data about each maximum were fit with a simple parabola. The resulting best fit positions are marked by the vertical lines in Figure 3, with MINOS uncertainties shown as the horizontal errorbar in the corresponding points above the data.

In contrast, at low magnetic field there is a surprising loss of asymmetry. The relaxation data at 20 mT as a function of

temperature is shown in Figure 4. The expected asymmetry, determined by a calibration run, is $\mathcal{A}_0 = 0.152(2)$ shown by the red dashed line, so there is a substantial “missing fraction”, i.e. a fraction of the implanted ${}^8\text{Li}$ whose spin has relaxed so quickly that its signal is wiped-out. The missing fraction is present at all temperatures, but it is largest in the vicinity of 100 K.

Based on the high field data and the field dependence of the relaxation at room temperature (see Appendix B), we also fit the relaxation at 20 mT with a biexponential, but unlike the 6.55 T data, the amplitude varies with T . The resulting fits have reduced $\chi^2 = 1.0$, and examples are shown as the blue curves in Figure 4. While not constant, f_s only varies from 29-50 %. In contrast, the amplitude is more strongly temperature dependent [see Section IV and the plot of the missing fraction $[\mathcal{A}_0 - A(T)]/\mathcal{A}_0$ in Figure 12b)]. From these fits, the $\lambda_i(T)$, shown in Figure 5, exhibit similar peaks to the high field rates. At such a low field, other relaxation mechanisms that are quenched in high magnetic fields may modify and even dominate the relaxation. The similarity in the T dependence suggests this is not the case. At 300 K, both rates are comparable in magnitude to 6.55 T. However, the two components do not correspond. It is very likely that the fast relaxation at high field becomes the missing fraction at 20 mT as suggested by the similar T dependence to the fractions, see Figure 12. Compared to λ_s at 6.55 T, the peaks in Figure 5 are shifted to substantially lower temperature as would be expected for thermally activated relaxation, given the much smaller ω_0 . Using a similar strategy as above, the peak temperatures (vertical lines in Figure 5) were determined by parabolic fits. Aside from the peaks, the background relaxation at low field is more independent of temperature, particularly below 50 K.

In a separate measurement, we implanted 25 keV ${}^8\text{Li}^+$ in the temperature range 55 – 450 K to test for migration back to

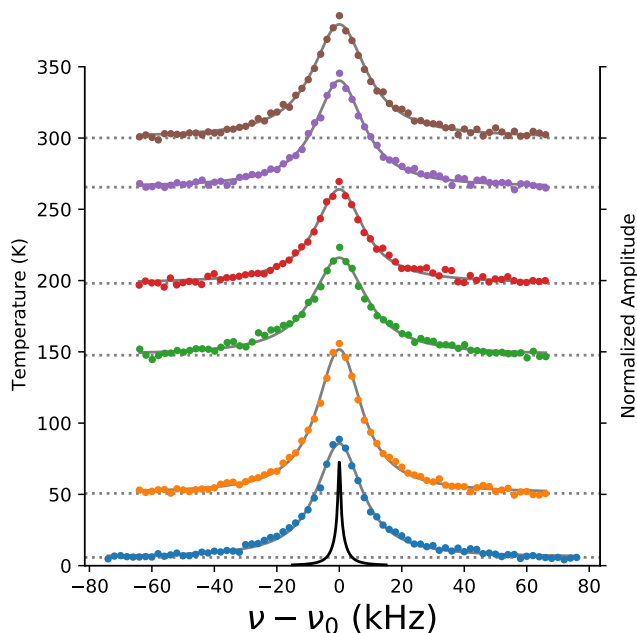


Figure 6. Single tone RF β -NMR spectra of $^8\text{Li}^+$ implanted in an α - SiO_2 single crystal with $B_0 = 6.55$ Tesla $\parallel c$. The large amplitude resonance is remarkably broad and not strongly temperature dependent. The baselines are offset to match the temperature label on the left. The black curve shows a calibration spectrum in MgO (scaled down by 2) for comparison.

the surface via the online alpha radiotracer method[4]. This technique uses the pair of alpha particles also produced in the ^8Li decay chain. The α s are strongly attenuated by the sample, so only decays occurring very near the surface produce α s that are detected. Ionic motion towards/away from the surface of even a few nanometers per $\tau_{1/2}$ produces an observable time-dependence in the alpha particle yield. In this case, we found no time-dependence of the alpha rates at any temperature, suggesting that at the scale of nm, the diffusion rate of implanted $^8\text{Li}^+$ in quartz is less than 1 nm/s even at 450 K. However, nanoscale diffusion does not always follow the intrinsic hop rate. For example, if the c -axis channels are blocked by defects every few nanometers, then ^8Li might exhibit very fast hopping without significant time evolution of the implantation profile.

Having summarized the relaxation data, in the next section we present the resonance spectra in high magnetic fields.

B. Resonance Spectra

Single tone RF spectra in high magnetic field are shown in Figure 6 normalized to the off-resonance time-average “baseline” asymmetry. They are well-described by a single Lorentzian (fit curves) resonance near the Larmor frequency without evident quadrupolar splitting. We estimate an ^8Li shift of about $-25(2.5)$ ppm (independent of T) relative to a calibration in MgO, typical of the small ^8Li shifts in nonmagnetic oxides. The line is unexpectedly broad, with a full-width at half-maximum

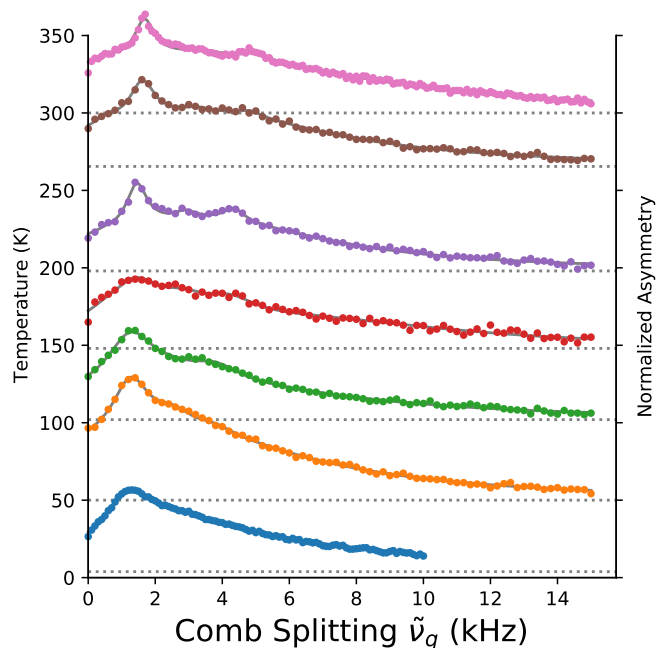


Figure 7. Quadrupolar RF comb β -NMR spectra of $^8\text{Li}^+$ implanted in an α - SiO_2 single crystal at $B_0 = 6.55$ $\parallel c$ Tesla. The comb is centered on the resonance in Figure 6 and the ordinate is the comb splitting parameter $\tilde{\nu}_q$. When this matches the characteristic splitting of an ^8Li site, a substantially enhanced resonance is observed. The baselines are offset to match the temperature label on the left.

(FWHM) of ~ 20 kHz independent of T . For comparison, we include the resonance in MgO in Figure 6 which, while it is about 10 times narrower than the quartz line, is still power broadened far above the instrumental limit[46]. The baseline asymmetry (and hence the resonance amplitude) depends on T through the SLR rate, so without normalization, the resonances are smaller in the region of the SLR peaks. At all T , the resonance amplitude is $\sim 40\%$ of the baseline asymmetry (full saturation). This is remarkably large for the breadth of the line and strongly suggests that the resonance is not a static lineshape. At room temperature, this is confirmed by a time-resolved hole-burning measurement that indicates a substantial effect of slow spectral dynamics of the ^8Li , i.e. the resonance condition is fluctuating on the timescale of 10 ms. This enhances the effect of the RF, amplifying the time-integrated resonances in Figure 6, as well as modifying the line shape.

Though no quadrupole splitting is evident in Figure 6, with the four frequency comb excitation, we find a resonance at finite splitting $\tilde{\nu}_q$. With the comb centred on the Lorentzian in Figure 6, spectra as a function of comb splitting parameter $\tilde{\nu}_q$ are shown in Figure 7. As the comb lines sweep through the broad spectrum in Figure 6, there will be a similarly broad signal centred at $\tilde{\nu}_q = 0$, and this is the case in Figure 7. However, superposed on this broad line, there is a resonant signal near 2 kHz together with its alias at three times this frequency. The four line satellite pattern corresponding to this value of ν_q overlaps the centre of the broad resonance in Figure 6 and, without the comb enhancement, is too weak to detect using the

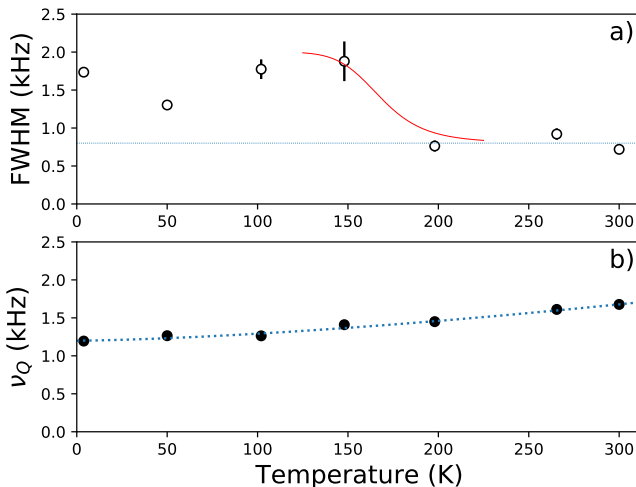


Figure 8. Temperature dependence of a) the linewidth of the narrow comb resonance and b) the position of the comb resonance ν_Q from fits to the spectra shown in Figure 7. The red curve shows a possible motional narrowing that would account for the drop in width above 150 K. The dashed curve in b) is the fit described in the text.

single tone RF. The comb resonance in Figure 7 is broad at low temperature but narrows substantially above 150 K where the ${}^8\text{Li}^+$ should be mobile. Careful inspection of the single tone spectra in Figure 6 suggests a small very sharp component superposed on the broad Lorentzian in this high temperature range. This may be the multiquantum resonance at the centre of the narrowed quadrupolar multiplet giving the comb resonance. Fitting the comb spectra to a sum of Lorentzians: narrow lines for the primary resonance and its aliases (see discussion) and a broad background (FWHM ~ 10 kHz) corresponding to the broad dynamic Lorentzian line in Figure 6 (curves in Figure 7), we obtain the line width and quadrupole frequency ν_Q plotted as a function of T in Figure 8.

IV. DISCUSSION

We begin with the high temperature regime, where we expect the implanted ${}^8\text{Li}^+$ to be diffusing. Accepting the conclusion that Li^+ motion is frozen below 150 K [28], we attribute the broad high temperature peaks in the SLR rates in Figures 3 and 5 to hopping of ${}^8\text{Li}^+$ along the channel. Assuming a simple BPP picture, the peak position occurs when the hop rate matches the Larmor frequency. At 6.55 T, the peaks in both fast and slow fractions are practically coincident. Presuming the fast component is missing at 20 mT, both fast and slow components at 20 mT in Figure 5 correspond to the high field slow component. The peak positions (temperatures) from the parabolic fits are shown on an Arrhenius scale in Figure 9. Treating the two components at 20 mT as independent measurements yields two different Arrhenius laws with barriers plotted in the inset of Figure 9. The prefactors (vertical intercept in Figure 9) are in the expected range [$8(5) \times 10^{12}$ (slow) and $1.2(8) \times 10^{11}$ (fast)], and thus do not exhibit any significant

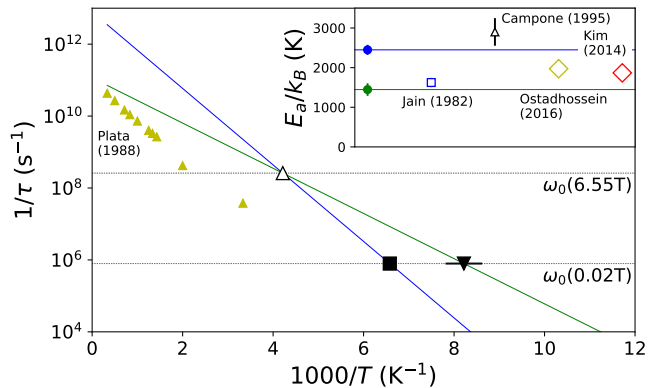


Figure 9. ${}^8\text{Li}^+$ hop rates determined from the high temperature SLR peak positions at the two fields (giving the NMR frequencies shown as horizontal lines) [open triangle from Figure 3a), closed symbols from Figure 5] with the resulting Arrhenius dependencies shown as the blue and green lines. Yellow triangles are calculated rates from Ref. 49. **Inset:** The barrier to hopping for Li^+ in $\alpha\text{-SiO}_2$ from the slopes in the main panel compared to values from the literature. The large diamonds are calculated [9, 48], while others are experimental [24, 47].

anomaly [38]. The slopes ($-E_a/k_B$) are in the range found in other measurements [24, 47] and calculations [9, 48] for the isolated Li^+ . It is difficult to obtain an absolute value of $1/\tau$ from the conductivity due to uncertainty in the ionic carrier concentration. Similarly, the prefactor $1/\tau_0$ is difficult to calculate, but Ref. 49 does report absolute theoretical hop rates at higher temperatures (yellow triangles in Figure 9). From these, one can see the slope is comparable to the steeper of our measurements, but the prefactor is an order of magnitude smaller. Though the two component character of the low field relaxation is clear in Figure 4, we do not know what distinguishes the components. Combined with substantial uncertainty in locating the relaxation peaks in Figure 5, we report the average of the two slopes [178(43) meV or $2.1(5) \times 10^3$ K] in Figure 9 as our best estimate of the hopping barrier for ${}^8\text{Li}^+$ in quartz.

Quite generally, the temperature and field dependence of the diffusive SLR rate is given by [35, 50]

$$\lambda_{\text{diff}} = C [J(\omega_0, \tau) + 4J(2\omega_0, \tau)], \quad (4)$$

where C is a scale factor determined by the nuclear spin coupling, and J is the fluctuation spectral density. The temperature dependence of $\lambda(T)$ arises from the correlation time $\tau(T)$ which we assume to follow an Arrhenius dependence as in Equation (1). In the case of an exponentially decaying autocorrelation, we have the BPP spectral density [37] appropriate to 3D diffusion,

$$J_{\text{BPP}}(\omega, \tau) = \frac{2\tau}{1 + (\omega\tau)^2}. \quad (5)$$

This does not have the correct asymptotic behavior for 1D diffusion as $\omega\tau \rightarrow 0$ [30, 51]. However, this is remedied by a simple heuristic factor,

$$J_{\text{1D}}(\omega, \tau) = \sqrt{1 + \frac{1}{\omega\tau}} \cdot J_{\text{BPP}}(\omega, \tau). \quad (6)$$

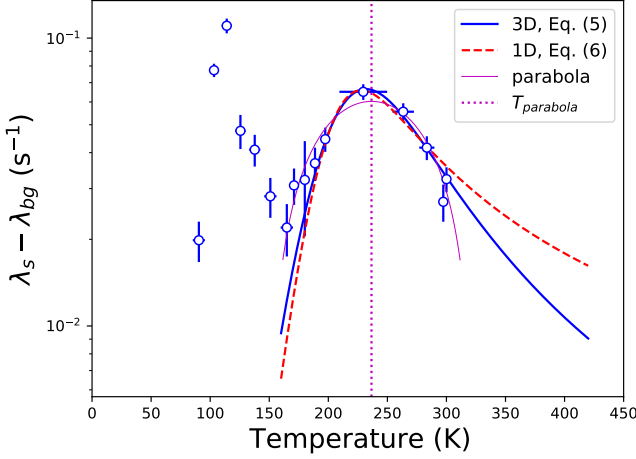


Figure 10. The relaxation rate of the slow component at $B_0 = 6.55$ T with the background rate subtracted compared to calculated model diffusive rates from Equation (4) (curves) using the BPP spectral density Equation (5) (blue) and the heuristic 1D function Equation (6) (red dashed). Also shown is the parabolic fit (purple) centred on the vertical dotted line which is used in Figure 9.

Both spectral densities produce a relaxation peak when $\omega\tau(T) \sim 1$. Beyond this, the width in temperature is determined by how fast the Arrhenius $1/\tau$ sweeps through the peak region. A larger prefactor $1/\tau_0$ requires a larger E_a and results in a narrower peak, while 1D diffusion yields a characteristically asymmetric peak with a weaker fall off at high temperature[35], a feature captured by Equation (6).

To compare these models to the data, we select the slow component at high magnetic field, which has the largest variation and the two peaks in $\lambda_s(T)$ are best separated. Subtracting the background rate (constant above 100 K), we get the relaxation rates shown in Figure 10. The two models each depend on 3 parameters: C in Equation (4) and the Arrhenius parameters. The latter two are highly correlated, so while the curves are not fits, they indicate that both models *could* fit the data quite well. The corresponding barriers are low [$E_a/k_B = 1430$ (3D) and 1650 K (1D)] and the intercepts required to match the peak width are $1/\tau_0 = 2$ and $9 \times 10^{11} \text{ s}^{-1}$, somewhat less than the analysis using both fields shown in Figure 9. From Figure 10, it is clear that distinguishing 1D diffusive relaxation requires a greater dynamic range of λ and a wider T range. Though the detailed shape of the peak (e.g., its width and symmetry) contain more information than the peak position alone, the ability to discern features characteristic of 1D is limited here by the other relaxation channels that give rise to the low temperature peak and the background rate. Given these limitations, the peak position analysis presented above remains a reasonable model-independent approach. With more beam time, the Arrhenius parameters could be better determined by measurements at several more magnetic fields.

A significant conclusion that can be drawn directly from the SLR data is that diffusive relaxation is not the only operative mechanism. From Figures 3 and 5, it is clear that both fast and slow rates have similar T dependencies, suggesting they share

a similar origin, with the distinction between λ_f and λ_s mostly one of scale. It appears reasonable to decompose the relaxation into three distinct processes,

$$\lambda(T) = \lambda_{\text{diff}} + \lambda_{\text{pk}} + \lambda_{\text{bg}}, \quad (7)$$

where λ_{diff} accounts for the high T broad diffusive peak discussed above [Equation (4)], λ_{pk} is the sharp lower T peak, and λ_{bg} is a background rate that is independent of T at low field, while at high field, it increases from a small low T value to plateau above ~ 50 K (dotted lines in Figures 3 and 5). The background rate is reminiscent of NMR relaxation due to dilute paramagnetic centers in wide band gap insulators, where it is due to the fluctuations of the unpaired electronic spin of the defects[52, 53]. At low T , the fluctuations are so slow that they are ineffective at relaxing the nuclei in high B_0 , but the fluctuation rate $1/T_1e$ increases via spin-lattice coupling with the thermally excited phonons until the low frequency tail of its spectral density overlaps the NMR frequency and it begins to cause relaxation. At low field, this can occur at a much lower T . The high T plateau is not as well understood, but it is likely a superposition of several broad features[52, 53]. We will return to consider the origin of the remaining term λ_{pk} below.

To obtain a more detailed understanding of the diffusive dynamics and to assist in interpreting the unexpected features of the data at lower T , we next consider the site of the implanted $^8\text{Li}^+$. In a crystal, the implanted ion generally stops in a vacant interstitial site, often a high symmetry crystallographic site. In some cases, multiple inequivalent sites are populated, some being metastable with a barrier to the lowest energy site in the unit cell. The NMR spectrum contains information about the site, particularly through the quadrupolar interaction which couples the ($I > 1/2$) spin of the nucleus to the local electric field gradient (EFG) tensor. The EFG is determined by the charge distribution surrounding the site, and the scale of the coupling is given by the product of the nuclear electric quadrupole moment (eQ) with the principal component of the EFG ($V_{zz} = eq$) defining the quadrupole frequency[54] for ^8Li as,

$$\nu_q = \frac{e^2 q Q}{4h}. \quad (8)$$

Usually this is much smaller than the Zeeman interaction with the applied field B_0 (i.e., $\nu_q \ll \nu_0$), and the quadrupolar coupling can be treated as a perturbation, which to first-order, splits the NMR line into a symmetric multiplet of $2I$ quadrupolar satellites corresponding to the $|\Delta m| = 1$ transitions among the $2I + 1$ states of the nuclear spin. For the present case, the satellite frequencies are given by

$$\nu_i = \nu_0 + n_i \frac{\nu_q}{4} \left(3 \cos^2 \theta - 1 + \eta \sin^2 \theta \cos 2\phi \right), \quad (9)$$

where $n_i = \pm 1 (\pm 3)$ for the inner(outer) lines; $\eta \in [0, 1]$ is the dimensionless asymmetry parameter of the EFG; and θ and ϕ are the polar and azimuthal angles of B_0 in the principal axis coordinate system of the EFG. This interaction is often the largest coupling of a quadrupolar nuclear spin to its crystalline environment. The RF comb spectra show resonances at finite

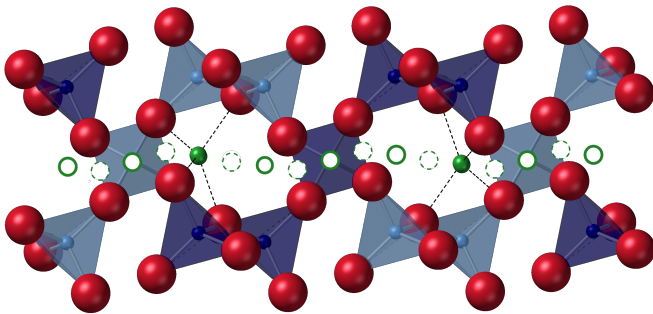


Figure 11. Side view of the c -axis channel in quartz showing occupied interstitial Li sites (green spheres), vacant sites (solid green circles). The dashed green circles indicate the metastable Li sites midway between adjacent stable sites. There are three minimum energy Li sites in each channel per c -axis lattice constant on the 2-fold axes $\perp c$ of the ideal structure. This axis rotates by 120° about c between adjacent sites. The double spiral of the linked SiO_4 are shown as the light and dark blue tetrahedra.

splitting $\tilde{\nu}_q$ (see Figure 7), yielding the ν_q characteristic of the corresponding ^8Li site. The measured value is much smaller than in either Al_2O_3 [45] or ZnO [40]. In part, this is due to the higher covalence of SiO_2 that makes the charge distribution more uniform. The T dependence of ν_q [plotted in Figure 8 b)] shows a clear *increase* with temperature, in contrast to the more common case of a decrease. The fit shown is $\nu_q(T) = \nu_{q0}(1+BT^{1.5})$ with the zero temperature quadrupole frequency $\nu_{q0} = 1.199(12)$ kHz and $B = 7.7(3) \times 10^{-5} \text{ K}^{-1.5}$. An increasing EFG is not unprecedented[55], but the relative change is quite large. This trend bridges the transition to mobility marked by the line narrowing, so it does not appear to be directly related to motional averaging. The T dependence of ν_q is primarily due to lattice vibrations, and the unusual variation found here may arise from the flexibility of the quartz structure to torsion of the SiO_4 tetrahedra[56].

Naturally occurring Li^+ impurities in α - SiO_2 occupy interstitial sites in the c -axis channels (see Figure 1). EPR of trapped holes[28] and electrons[57] in the vicinity of interstitial Li^+ show hyperfine splittings from the ^7Li nuclear spin. The site determined by analyzing these splittings[28, 58] is near the central axis of the channel [c -axis edge of the unit cell in Figure 1] where it intersects the two-fold crystallographic axis ($\perp c$) that bridges the channel joining two Si atoms on opposite sides (abbreviated below as TFA). This site is quasitetrahedrally coordinated by oxygen bonded to the two Si[28]. There are three such sites in the unit cell, equally spaced along c , but with the bridging TFA rotated by 120° about c . The array of such sites is not linear but describes a tight helix winding along c [49], as illustrated by the filled green circles and spheres in Figure 11. Without the charge of the unpaired electron (that gives the EPR signal), the site of *isolated* Li^+ is difficult to determine experimentally[59] and may differ, but calculations find a similar quasi-tetrahedral in-channel site[9, 48, 60, 61]. The EFG at the nucleus is predominantly due to the nearby charge distribution, as it falls as r^{-3} . Moreover, it is zero by symmetry when the charge distribution is cubic. Thus, qualitatively, one can expect the quasi-tetrahedral site to have a

Table I. GIPAW calculated quadrupole parameters for the dilute $^8\text{Li}^+$ from the $3 \times 3 \times 4$ supercell in the two sites.

Site	ν_q (kHz)	η
Stable	-29	0.50
Metastable	-58	0.12

small EFG.

Using supercell density functional theory (DFT) calculations [see Appendix C for details], we confirm the lowest energy site is as described above. However, midway between neighboring minimum energy sites, there is another shallow minimum ~ 0.13 eV higher in energy which is also quasi-tetrahedrally coordinated by oxygen, suggesting the hopping barrier may include a metastable transition state. This may be the ‘B’ transition site referred to in Ref. 9. The stable site is a Wyckoff $3a$ site along the TFA, with a ~ 0.12 Å transverse offset from the channel center. Along the channel, the metastable site is midway between adjacent stable sites and has a similar transverse offset ~ 0.11 Å, defining the radius of the helical path depicted in Figure 11.

From the relaxed structure at these two sites, we use GIPAW[62, 63] to estimate the EFG at the Li nucleus. This method reproduces the EFG at ^{17}O in SiO_2 quite well[64, 65]. The calculated quadrupole parameters for dilute $^8\text{Li}^+$ are summarized in Table I. While the EFG at the Li site is $\sim 50\times$ smaller than at oxygen, ν_q is still much larger than the experimental value. Comparison of GIPAW EFGs with experiment over a broad range of materials show substantial scatter, particularly for light elements, and there is an effective uncertainty on the calculated values in Table I on the order of 50 kHz[66]. Based on this, the observed comb resonance is consistent with the stable channel site. The site symmetry determines the EFG orientation which is reliably calculated by GIPAW. For the stable site, the EFG principal axis is along the TFA rotating by 120° about c from one site to the next along the channel. This means that, for the high field spectra shown in Equation (9), $\theta = 90^\circ$. With a very small barrier to stability, the metastable site probably has a negligible population on average. However, it may be occupied briefly by the hopping ion. Here the EFG is about twice as large (with a smaller η), and it is no longer in the ab plane. It would be interesting to revisit the calculations of Ref. 49 including the metastable position to see if better agreement with the experiment could be obtained.

The best resolved comb spectra in Figure 7 are at high T . The low T spectrum, where ^8Li is frozen, is still peaked at ν_q but is substantially broader. In part, this is due to the 3 distinct orientations of the EFG in the 3 randomly populated stable sites, resulting in 3 distinct EFG angles in Equation (9) which split the resonances further. This is analogous to the 3-fold splitting of the ^{29}Si NMR from 3 distinct orientations of the SiO_4 tetrahedra[65]. Another unrelated source of broadening originates in the magnetic interaction with other spin-bearing nuclei. This “dipolar coupling” also broadens the resonance to an extent determined by the abundance and magnitude of the nuclear magnetic moments. In SiO_2 these are very dilute (see

Table II. Spin-bearing nuclei in the α -SiO₂ crystal. For each isotope, its concentration (relative to Si), the magnitude of its nuclear dipole moment μ (in nuclear magnetons μ_N), along with its spin quantum number I , is listed. Note that the quoted ^8Li concentration corresponds to its estimated maximum value during the experiment.

Isotope	Concentration (ppm)	μ (μ_N)	Spin I
^{29}Si	~ 47000	-0.555	$1/2$
^{17}O	~ 760	-1.894	$5/2$
^1H	< 2500	$+2.793$	$1/2$
^{27}Al	< 5	$+3.642$	$5/2$
^8Li	< 0.0001	$+1.653$	2

Table II), so dipolar broadening is not significant. For example, at room temperature, the ^{29}Si NMR linewidth is only ~ 0.35 kHz[65], notably much less than our widths.

Upon warming, the comb resonance becomes narrower and better defined above 150 K (see Figure 8), suggesting the corresponding fraction of ^8Li is mobile. In the fast diffusion limit, the EFG is averaged and there is a single quadrupole multiplet. Motional narrowing occurs when the rate of site-to-site hopping exceeds the frequency scale of the broadening (kHz). At even higher T , when hopping is much faster, it will cause the SLR rate peak λ_{diff} . The motional SLR is almost certainly quadrupolar (from the random modulation of the quadrupole interaction due to hopping). Such relaxation is generally anisotropic, since the relevant fluctuating terms depend on the direction of B_0 , so they should be different in the 20 mT data. The square magnitude of the fluctuating coupling determines C in Equation (4) and thus the height of the SLR peak. Indeed, the observed heights require a fluctuating coupling on the kHz scale, consistent with the observed ν_q .

In contrast, the broad resonance in Figure 6 shows no substantial change over a temperature range that spans this onset of mobility, so this fraction is not diffusing. Its amplitude is enhanced dynamically by spectral diffusion on the second timescale [see Appendix D]. The linewidth is nearly the same at 5 K (lowest spectrum in Figure 6) and room temperature. The lack of T dependence to the resonance suggests the spectral dynamics are not thermal. Rather, they are probably caused by implantation-related excitations. Among these, STE are quite long-lived[67], but the RIC persists much longer[22, 24]. Fluctuations from more distant long-lived excitations might account for the slow fluctuations seen by this immobile fraction of the implanted $^8\text{Li}^+$.

Both the relaxation and resonances are multicomponent. The high field biexponential suggests two distinct populations of ^8Li [68], but the low field missing fraction shows that there are at least three. The sharp comb resonance in Figure 7 coexists with the large broad resonance in Figure 6. The latter is substantially wider than the entire multiplet pattern at the comb ν_q , so it must correspond to a distinct environment. Hole-burning shows the broad resonance in Figure 6 corresponds to the slow relaxing component; however, since it does not completely depolarize the remaining signal, there are also three components in the resonances: the comb resonance, the broad dynamic resonance and another (slow-relaxing) component

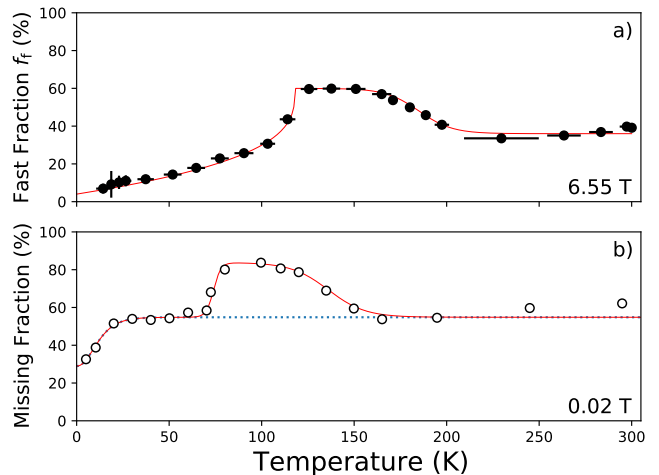


Figure 12. a) The fraction of the signal that relaxes rapidly, f_f at 6.55 T as a function of temperature from the global biexponential fit. b) The missing fraction at 0.02 T as a function of temperature. The red curves are empirical fits.

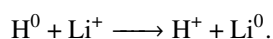
unaffected by the resonant RF. Both the rates [Figure 3] and the relative fractions [Figure 12 a)] evolve with T . The temperature dependence of the fraction f_f is considerably more complicated than for a thermally activated site change[69]. More complex T dependence can arise when there are multiple distinct final state defect configurations. For example, when the positive muon μ^+ is implanted into semiconductors it can form muonium — an isolated atomic defect (H atom analog) — that can exhibit distinct crystallographic and charge states that evolve with T [70, 71]. Another well-known phenomenon for the muon is diffusion and trapping[72], where dilute static defects within the structure provide an attractive trapping potential for the implanted ion. Our sample is sufficiently pure that the vast majority of the randomly stopped $^8\text{Li}^+$ will not be in the vicinity of defects such as an Al impurity. Even for the much more abundant hydrogen, at the estimated maximum concentration, the average distance between H impurities along the channel is about 70 nm. While substitutional Al acts as a trap, interstitial H^+ would be a channel blocker. There are a number of other hydrogenic defect configurations, including some OH defects which can trap Li^+ [73]. There is also evidence for unidentified shallow Li^+ trap sites[24, 74].

In the simplest case, the biexponential fractions might correspond to freely diffusing and trapped $^8\text{Li}^+$. The diffusing fraction corresponds to the sharp, motionally narrowed comb resonance. The strong hole-burning effect at late times [Appendix D] indicates that the broad line (not the sharp comb line) corresponds to the slow relaxation, hence the diffusing fraction is the *fast* relaxing component at 300 K. The decrease in this fraction f_f above 150 K [see Figure 12 a)], coinciding with the known mobility onset of Li^+ in the channel, could then be due to diffusion to traps (i.e., conversion from fast to slow relaxing populations). However, trapping is incomplete as $\sim 40\%$ of the signal remains fast relaxing at 300 K. This suggests there is a population of $^8\text{Li}^+$ in trap-free channel segments

bounded by channel blockers that limit the range of diffusion, consistent with the α radiotracer measurement. The presence of the λ_{diff} peak in the slow component appears inconsistent with this interpretation, but it suggests the reverse process (detrapping) occurs for at least some shallow traps in this T range, so that repeated cycles of diffusion and trapping may occur. A stochastic model of relaxation (without detrapping) is given in Appendix E. It shows that the average effect of trapping is to interpolate between the characteristic relaxations of the free and trapped states. A more sophisticated model along these lines (i.e., including an untrapped fraction, thermal detrapping, and possibly several trap energies) might be able to account for the T dependence above 150 K.

Thus far, a single consistent assignment of the fractions based on the above appears untenable, as there are substantial changes at low T where ${}^8\text{Li}^+$ cannot be mobile. Based on the behavior of the implanted muon[70, 71], here we consider whether formation of the neutral ${}^8\text{Li}^0$ could account for the features of the data below 150 K. This possibility is suggested by the EPR of Li^0 in quartz, and we begin with a brief summary of what is known. Formation of Li^0 is enabled by intense Xray irradiation at low temperature[57], producing a uniform distribution of radiolytic electrons to react with the isolated Li^+ . The unpaired electron yields the EPR which shows small hyperfine splittings. Electron-nucleus double resonance (ENDOR) confirms these are from the stable ${}^7\text{Li}$ nucleus. Detailed analysis of the EPR shows that Li is at the channel site with the unpaired electron primarily located on the neighboring Si[28, 58]. The EPR is only observed at low temperature and its intensity decreases in two annealing steps: at 109 K, the signal is reduced by about 20%, and above 187 K, the remaining signal is rapidly wiped out[57]. Both annealing steps (but particularly the latter) are accompanied by luminescence[75], indicating that destruction of Li^0 is part of a charge recombination process.

In contrast to the stable Li^0 , the kinetics of formation (electron capture) would play an important role for the implanted ${}^8\text{Li}^+$ which stops randomly, almost always isolated from other pre-existing (dilute) defects. It can then trap an electron from its own (certainly not uniform) radiolysis track to produce ${}^8\text{Li}^0$. This is analogous to the formation of muonium in quartz which depends on the implanted μ^+ capturing such an electron[76, 77]. Neutralization then depends on the distribution of radiolysis electrons, their mobility, and competing processes such as recombination, and will, as a result, be T dependent. Neither electrons nor holes are polaronic in quartz[78, 79], so they are quite mobile, but they will often be trapped by other defects. The ${}^8\text{Li}$ lifetime is much longer than the $2.2\ \mu\text{s}$ of the muon, so the neutralizing electron may even originate from shallow traps rather than from radiolysis directly. Most such traps are immobile[80, 81], including the self-trapped exciton (STE)[82], and some are sufficiently stable to be useful in geochronology[83]. However, radiolytically liberated atomic hydrogen is an electron trap that mobilizes in the channel at $\sim 100\ \text{K}$ [84, 85]. Hydrogen may thus be able to shuttle an electron to the ${}^8\text{Li}^+$ in a charge exchange reaction,



We are not aware of any case where the β -NMR signal of

paramagnetic ${}^8\text{Li}^0$ has been observed in a solid, so we now consider how it might manifest itself.

The hyperfine coupling to the electron spin provides a substantial effective magnetic field at the probe nucleus. From the EPR, we expect a hyperfine coupling $A_c \sim 0.95\ \text{MHz}$ for ${}^8\text{Li}^0$, so the β -NMR should be split (magnetically) into two ENDOR lines at $\nu_0 \pm A_c/2$. This splitting is much larger than the frequency range in Figure 6. However, it is unlikely the hyperfine field is static on the timescale of the measurement. For stable Li^0 , the electron T_{1e} at the EPR field (0.33 T) is very long relative to the EPR frequency (9.3 GHz)[57]. Though values are not reported, this may be on the microsecond timescale, and T_{1e} will only be longer at our much higher B_0 . Fluctuations of the hyperfine field at a rate comparable to the splitting would instead produce a broad line shifted from ν_0 by the thermodynamic polarization of the electron spin.

The hyperfine field would also enhance the relaxation rate. At low field, such fast relaxation could account for the large missing fraction in Figure 12 b) which shows a clear similarity with $f_f(T)$ at high field, but the plateau region is shifted down, suggesting field-dependent spin relaxation controls the stepwise changes in the fractions. It could also account for the sharp peak in the high field relaxation λ_{pk} , which appears closely related to the T dependence of the fractions. Both $\lambda_f(T)$ and $\lambda_s(T)$ are described well by the decomposition of Equation (7), but the position of λ_{pk} differs. The slow component peak coincides with the sharp increase in f_f , suggesting it is due to charge and spin exchange fluctuations of neutralization. Similarly, in low field the peaks (both slow and fast) coincide with the sharp upward step in the missing fraction, confirming their relation to the slow component in high field. In contrast, the fast component λ_{pk} occurs in the middle of the plateau just below the onset of the decrease in f_f . While this is substantially below the 187 K annealing of the EPR signal, it is probably connected with annihilation of the neutral. The $\sim 2.8\ \text{eV}$ luminescence light associated with this annealing[86, 87] is very similar to the light emitted from annihilation of the STE[67], suggesting one recombination pathway for the Li-trapped electron proceeds via the STE, which may act as a long-lived (milliseconds at 100 K) transition state bottleneck due to its triplet character[67, 88, 89]. Magnetic field fluctuations from such an STE in the vicinity of ${}^8\text{Li}^+$ could provide an additional mechanism for λ_{pk} . The neutralizing electron probably also acts as a trap, inhibiting hopping of the ${}^8\text{Li}^0$, which becomes mobile once ionized.

It is thus plausible that neutral ${}^8\text{Li}^0$ exists over a narrow range of temperatures between ~ 75 and 150 K and accounts for the complex T dependence of the relaxation in this range. However, it would be much more compelling to have a direct confirmation by measuring its hyperfine splitting. This will certainly be difficult and likely will require the development of new methods. In the meantime, by repeating these measurements on a crystal with a substantially lower H content, we might confirm an essential role for H in formation of the neutral and/or in λ_{pk} .

V. SUMMARY

Having set out to study 1D diffusion of implanted $^8\text{Li}^+$ in the channels of $\alpha\text{-SiO}_2$, we find the situation is more complex than expected and very different from other oxide insulators where $^8\text{Li}^+$ is immobile (e.g., MgO [90], Al_2O_3 [45] and ZnO [40]), while it bears some similarities to the 1D diffusion in rutile TiO_2 [3]. The SLR is fast and strongly temperature dependent with a broad diffusive peak above 200 K and a second more prominent relaxation peak at lower temperature. The diffusive relaxation yields a mean activation barrier of 178(43) meV for isolated Li^+ , in agreement with the range of other measurements and calculations. The range over which it is the dominant relaxation mechanism limits the ability to discern characteristic features of 1D diffusion. At 6.55 T, the ^8Li NMR spectrum has two observed components, a large amplitude broad resonance and a quadrupolar multiplet that is only revealed by an RF comb excitation, while a third fraction has an unobserved resonance. The quadrupole splitting is surprisingly small and increases with temperature. Comparison of ν_q with DFT calculations confirms the Wyckoff $3a$ in-channel interstitial site for $^8\text{Li}^+$.

To account for many unexpected features of the data between 75 and 150 K, it is suggested that a fraction of the implanted ions form neutral Li^0 by trapping a radiolysis electron. Formation of the neutral should be quite general across a wide-range of insulating materials, and the phenomenology reported here gives an indication of how it might appear in the β -NMR data. More extensive hole-burning measurements and a careful search for the hyperfine splitting of Li^0 would help to test this hypothesis. Depositing thin electrodes on the crystal to modulate the neutralization process via application of an electric field would also help to confirm the neutral. With some knowledge of its binding energy, spectroscopic confirmation might be obtained by illuminating the sample during the β -NMR measurement to alter its electronic state directly.

ACKNOWLEDGMENTS

We are grateful to R. Abasalti, D. Arseneau, B. Hitti, B. Smith, and D. Vyas for technical assistance. This work was supported by NSERC Discovery grants, NSERC CREATE IsoSiM fellowships (A.C. and R.M.L.M.), and SBQMI QuEST fellowships (D.F., V.L.K., and J.O.T.). This work was, in part, supported by funding from the Max Planck-UBC-UTokyo Center for Quantum Materials and the Canada First Research Excellence Fund, Quantum Materials and Future Technologies Program. We thank D. Ceresoli, J. Adelman, K. Foyevtsova, P. Macau, and I. Elfimov for help with the DFT calculations. Structural figures were made with CrystalMaker. Additionally, we thank Y. Qi and S.-Y. Kim for some clarification of Ref. 9. W.A.M. acknowledges the hospitality of LNCMI Grenoble for part of this work.

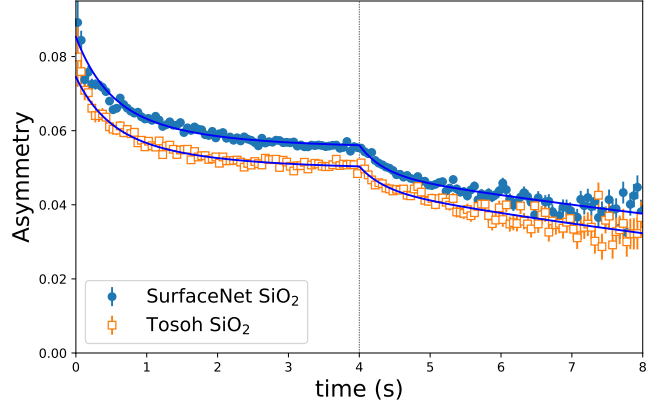


Figure 13. Spin relaxation of $^8\text{Li}^+$ implanted into two different samples of SiO_2 at room temperature and 6.55 T. The similarity between the samples confirms that the relaxation is typical of high purity quartz.

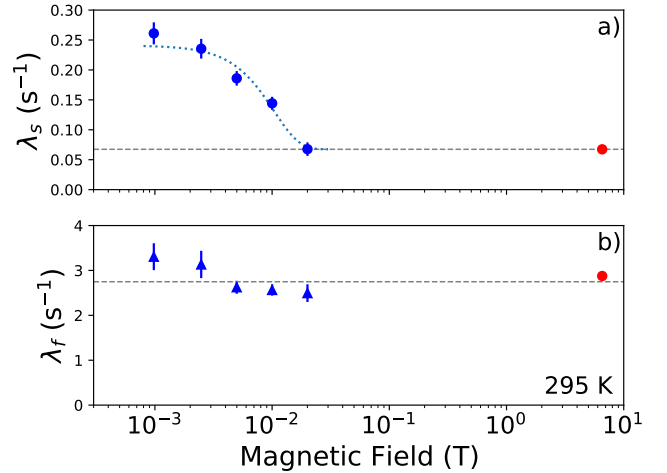


Figure 14. Rates from biexponential fits to the relaxation as a function of applied field at 295 K with a shared fraction f_s . At the lowest fields, the amplitude is further reduced. The red points are the high field data where there is no missing fraction. The horizontal lines show the rates at 20 mT are similar to those at 6.55 T, though the amplitude is significantly reduced.

Appendix A: Sample Comparison

At high field, we compare the relaxation data in the two quartz samples from different sources at 6.55 T and 300 K, see Figure 13. The data are not artificially offset, and the difference in amplitude is within the expected range of variability as the data were not taken in the same year. The similarity of the data indicates that the relaxation in the crystal presented in the main text is not sample specific, but appears characteristic of high purity quartz.

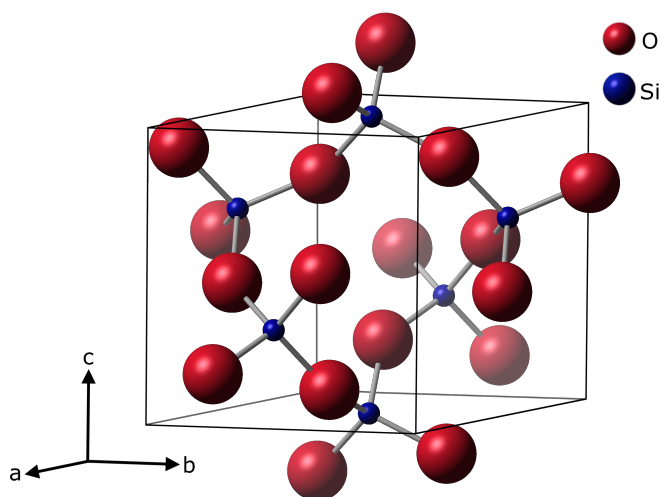


Figure 15. The conventional trapezoidal unit cell of α -SiO₂ (space group 152/154 depending on handedness) containing 3 formula units shown here for the Si atom in the basal plane at fractional coordinates (0.53, 0.53, 0.0). The central axis of the channel in Figure 1 corresponds to the vertical (c) unit cell edges. The room temperature lattice constants are $a = b = 4.91239(4)$ Å and $c = 5.40385(7)$ Å[91], with angles $\alpha = \beta = 90^\circ$ and $\gamma = 120^\circ$.

Appendix B: Field Dependence of the Relaxation at 300 K

At 295 K, the relaxation was measured as a function of B_0 in the low field regime. The data can be fit (reduced $\chi^2 = 1.1$) with a biexponential with a shared fraction $f_f = 0.704(8)$. The resulting rates (shown in Figure 14) demonstrate that the remnant signal has relaxation rates at 20 mT comparable to those at much higher field, despite the much smaller overall amplitude. The horizontal dashed lines are the average of the high field and 20 mT values. Here the relaxation is largely λ_{bg} which is probably magnetic rather than quadrupolar in origin. Below 20 mT, the rate of the slow component climbs, while the fast component remains relatively field independent. The similarity of rates suggests that (at room temperature) the same mechanism is predominant above about 20 mT, while at lower field an additional channel appears to dominate for the slow component.

Appendix C: Density Functional Theory Calculations

For the DFT calculations, we used QUANTUM ESPRESSO [92–94] with Troullier-Martins[95] norm-conserving pseudopotentials optimized for solid state NMR calculations[96]. We constructed supercells based on the conventional unit cell shown in Figure 15. To obtain a calculated EFG comparable to experiment, we fixed the lattice constants at the experimental values and allowed the system to relax with a constant unit cell volume. The kinetic energy cutoff for wavefunctions was 80 Ry, while for the charge density and potential 320 Ry was used. The energetic convergence threshold for self-consistency was set to 10^{-10} Ry and the mixing factor (beta) was 0.5. We modeled the

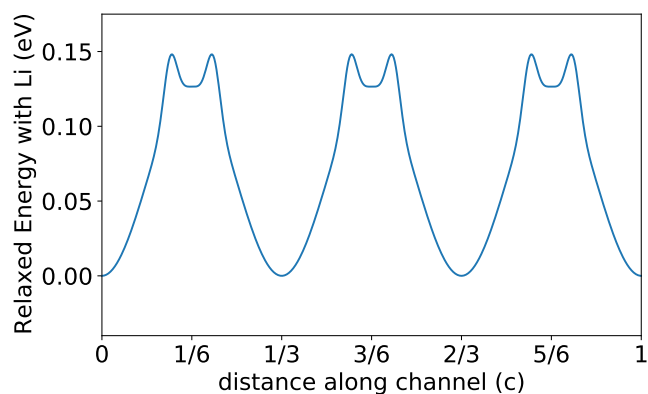


Figure 16. Schematic potential barrier for dilute Li⁺ along the channel in α -SiO₂ based on the two relaxed site energies in a $3 \times 3 \times 4$ supercell.

Li⁺ in two ways: the ion with a uniform compensating (jellium) charge and a neutral Li atom. Both gave similar results as expected[97], and only the former are reported here. We made no effort to try to model the metastable neutral Li⁰. To find the lowest energy sites, a sampling of initial Li coordinates were run with a smaller $2 \times 2 \times 2$ supercell (73 atoms) and less stringent convergence criteria. For the final energies and EFG, the calculation used a $4 \times 4 \times 4$ reciprocal space grid with no offset[98] and a $3 \times 3 \times 4$ supercell (325 atoms) to approximate the dilute limit (Li at ~ 9300 ppm relative to Si). The EFG calculation used the GIPAW implementation[62] packaged with QUANTUM ESPRESSO. The extent of the lattice relaxation around the interstitial Li was quantified by the magnitude of the displacement vector from relaxed supercells with and without Li⁺. Only the first few near-neighbour shells showed appreciable relaxation with all displacements less than 0.16 Å.

Appendix D: Hole Burning

A hole-burning experiment was done at 295 K and 6.55 T. With pulsed beam, the RF at the center of the broad line in Figure 6 is switched on at a specific time relative to the beam pulse. Any ⁸Li resonant with the RF will be depolarized in ms, leading to a sharp downward step Δ_{RF} in the time differential asymmetry with a 10 ms time-resolution. Much slower spectral diffusion brings other ⁸Li onto resonance over time leading to an apparent relaxation much faster than the SLR rate seen in the absence of RF. When the stochastic spectral diffusion of the resonance frequency occurs in many small steps, the resulting hole-burning relaxation is often of a stretched exponential form $\propto \exp(-\sqrt{\lambda_{RF} - t_{RF}})$. The data and fits together with a calibration run without RF are shown in Figure 17. The spectral diffusion relaxation is clearly a strong effect and will amplify the corresponding time-integral resonance in Figure 6 by at least a factor of 10. The spectral diffusion relaxation also confirms that there are slow fluctuations of the environment of a significant fraction of the ⁸Li in addition to the fast fluctuations that give rise to the diffusive SLR.

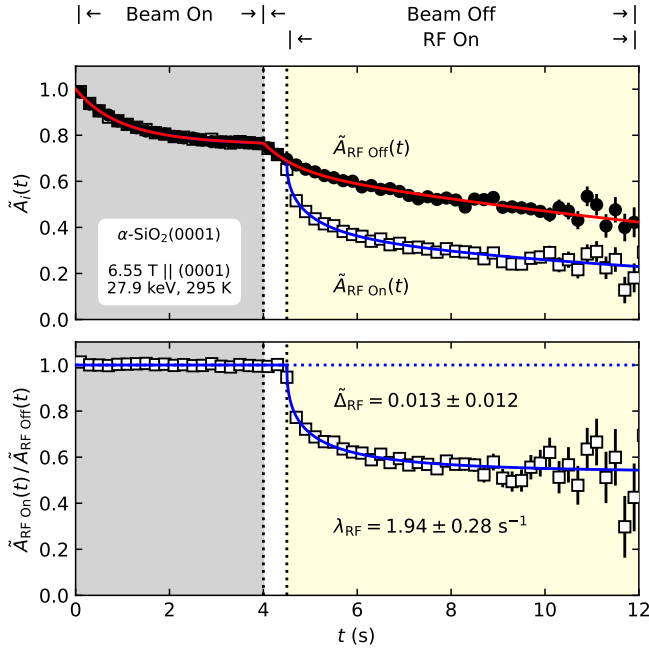


Figure 17. Hole-burning measurement at 6.55 T and 295 K. The single tone RF excitation at the centre of the resonance is turned on 0.5 s after the end of the beam pulse.

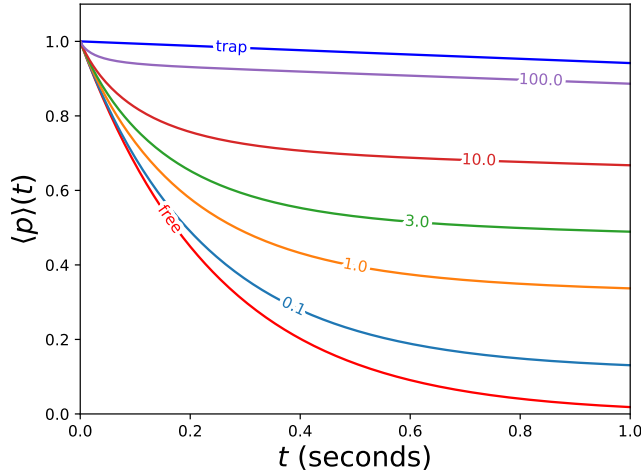


Figure 18. The average spin relaxation for a stochastic model of 1D diffusion and trapping with trap concentration 2500 ppm. The diffusing fraction is assumed to relax rapidly while the trapped fraction is slow. The average polarization from Equation (E1) is labelled by the hop rate W in kHz and shows a characteristic interpolation between the free and trapped relaxation functions. No detrapping is included.

Appendix E: Diffusion and Trapping in 1D

Here we illustrate the behavior of the depolarization function from a stochastic model of trapping in 1D. Defining $f(t)$ as the freely diffusing fraction at time t , the “survival fraction” in the argot of survival analysis. Let $\eta(t) = -df/dt$ be the probability per unit time that a diffuser is trapped in time interval $(t, t + dt)$. Movaghar *et al.*[99] considered 1D diffusion and trapping in some detail. Here we use their expression for the ‘First Passage Time’ estimate for f in 1D, namely,

$$\begin{aligned} f_{\text{FPT}} &= f_0 \left(1 - \int_0^t d\tau \eta(\tau) \right) \\ &= f_0 \exp \left(-x \int_0^t d\tau 2W e^{-2W\tau} [I_0(2W\tau) + I_1(2W\tau)] \right), \end{aligned}$$

where $I_{0,1}$ are modified Bessel functions, W is the hop rate and x is the relative concentration of the trap sites. Next we assume the trapped and free ions have characteristic single exponential relaxation functions, p_{free} and p_{trap} , with rates $\lambda_{\text{free}} = 4$ and $\lambda_{\text{trap}} = 0.06\ s^{-1}$ based on the 6.55 T data at about 200 K, and then we apply the stochastic trapping model[100] to obtain the average relaxation function $\langle p \rangle$,

$$\langle p \rangle = f(t)p_{\text{free}}(t) + \int_0^t d\tau \eta(\tau)p_{\text{free}}(\tau)p_{\text{trap}}(t - \tau). \quad (\text{E1})$$

Assuming a negligible initial trapped fraction $f_0 = 1$ and a trap concentration appropriate to hydrogen, numeric integration gives the results shown in Figure 18. The average $\langle p \rangle$ interpolates between p_{free} and p_{trap} for relatively low hop rates at this concentration of traps. Qualitatively, it resembles a biexponential where, as the hop rate increases, the fast fraction diminishes in amplitude and slows in rate before increasing in rate again.

[1] A. M. Glazer, Confusion over the description of the quartz structure yet again, *J. Appl. Crystallogr.* **51**, 915 (2018).

[2] D. Yogeve-Einot and D. Avnir, The temperature-dependent optical activity of quartz: from Le Châtelier to chirality measures, *Tetrahedron: Asymmetry* **17**, 2723 (2006).

[3] R. M. L. McFadden, T. J. Buck, A. Chatzichristos, C.-C. Chen, K. H. Chow, D. L. Cortie, M. H. Dehn, V. L. Karner, D. Koumoulis, C. D. P. Levy, C. Li, I. McKenzie, R. Merkle, G. D. Morris, M. R. Pearson, Z. Salman, D. Samuelis, M. Stachura, J. Xiao, J. Maier, R. F. Kiefl, and W. A. MacFarlane, Microscopic dynamics of Li^+ in rutile TiO_2 revealed by

- ^8Li β -detected nuclear magnetic resonance, *Chem. Mater.* **29**, 10187 (2017).
- [4] A. Chatzichristos, R. M. L. McFadden, M. H. Dehn, S. R. Dunsiger, D. Fujimoto, V. L. Karner, I. McKenzie, G. D. Morris, M. R. Pearson, M. Stachura, J. Sugiyama, J. O. Ticknor, W. A. MacFarlane, and R. F. Kiefl, Bi-arrhenius diffusion and surface trapping of $^8\text{Li}^+$ in rutile TiO_2 , *Phys. Rev. Lett.* **123**, 095901 (2019).
- [5] J. Verhoogen, Ionic diffusion and electrical conductivity in quartz, *Am. Mineral.* **37**, 637 (1952).
- [6] H. E. Wenden, Ionic Diffusion and the Properties of Quartz I. The Direct Current Resistivity, *Am. Mineral.* **42**, 859 (1957).
- [7] K. Kushida, K. Kuriyama, and T. Nozaki, Hundred-micron-sized all-solid-state Li secondary battery arrays embedded in a Si substrate, *Appl. Phys. Lett.* **81**, 5066 (2002).
- [8] C. K. Chan, R. Ruffo, S. S. Hong, and Y. Cui, Surface chemistry and morphology of the solid electrolyte interphase on silicon nanowire lithium-ion battery anodes, *J. Power Sources* **189**, 1132 (2009).
- [9] S.-Y. Kim and Y. Qi, Property evolution of Al_2O_3 coated and uncoated Si electrodes: A first principles investigation, *J. Electrochem. Soc.* **161**, F3137 (2014).
- [10] Y. Zhang, Y. Li, Z. Wang, and K. Zhao, Lithiation of SiO_2 in Li-ion batteries: In situ transmission electron microscopy experiments and theoretical studies, *Nano Lett.* **14**, 7161 (2014).
- [11] J. Götze, Y. Pan, and A. Müller, Mineralogy and mineral chemistry of quartz: A review, *Mineral. Mag.* **85**, 639 (2021).
- [12] P. R. Phelps and C.-T. A. Lee, Extreme lithium isotope fractionation in quartz from the Stewart pegmatite, *Geochim. Cosmochim. Acta* **336**, 208 (2022).
- [13] J. C. Brice, Crystals for quartz resonators, *Rev. Mod. Phys.* **57**, 105 (1985).
- [14] E. H. Snow and P. Gibbs, Dielectric loss due to impurity cation migration in α quartz, *J. Appl. Phys.* **35**, 2368 (1964).
- [15] J. Martin, Acoustic loss in cultured quartz, in *Proceedings of 1996 IEEE International Frequency Control Symposium*, IEEE Ultrasonics, Ferroelectrics, and Frequency Control Society (IEEE, Honolulu, HI, USA, 1996) pp. 170–178.
- [16] J. Martin, Electrodiffusion (sweeping) of ions in quartz – a review, *IEEE Trans. Ultrason. Ferroelectr. Freq. Control* **35**, 288 (1988).
- [17] P. S. Burada, P. Hänggi, F. Marchesoni, G. Schmid, and P. Talkner, Diffusion in confined geometries, *ChemPhysChem* **10**, 45 (2009).
- [18] A. Chatzichristos and J. Hassan, Current understanding of water properties inside carbon nanotubes, *Nanomater.* **12**, 174 (2022).
- [19] H. van Beijeren, K. W. Kehr, and R. Kutner, Diffusion in concentrated lattice gases III. tracer diffusion on a one-dimensional lattice, *Phys. Rev. B* **28**, 5711 (1983).
- [20] S. M. Abel, Y.-L. S. Tse, and H. C. Andersen, Kinetic theories of dynamics and persistent caging in a one-dimensional lattice gas, *Proc. Natl. Acad. Sci. U.S.A.* **106**, 15142 (2009).
- [21] Q.-H. Wei, C. Bechinger, and P. Leiderer, Single-file diffusion of colloids in one-dimensional channels, *Science* **287**, 625 (2000).
- [22] R. C. Hughes, Electronic and ionic charge carriers in irradiated single crystal and fused quartz, *Radiat. Eff.* **26**, 225 (1975).
- [23] H. Bahadur, Radiation induced modification of impurity-related point defects in crystalline quartz – a review, *Cryst. Res. Technol.* **41**, 631 (2006).
- [24] H. Jain and A. S. Nowick, Radiation-induced conductivity in quartz crystals, *J. Appl. Phys.* **53**, 485 (1982).
- [25] M. Martini, G. Spinolo, and A. Vedda, Radiation-induced conductivity of as-grown and electrodiffused quartz, *J. Appl. Phys.* **60**, 1705 (1986).
- [26] T. Miyazaki, N. Kato, K. Fueki, and N. Ohshima, Anisotropic electrical conductivity in quartz during γ -irradiation, *J. Am. Ceram. Soc.* **72**, 1289 (1989).
- [27] D. M. Follstaedt and P. M. Richards, NMR relaxation in the superionic conductor β - LiAlSiO_4 , *Phys. Rev. Lett.* **37**, 1571 (1976).
- [28] J. A. Weil, A review of electron spin spectroscopy and its application to the study of paramagnetic defects in crystalline quartz, *Phys. Chem. Miner.* **10**, 149 (1984).
- [29] J. B. Boyce and B. A. Huberman, Superionic conductors: Transitions, structures, dynamics, *Phys. Rep.* **51**, 189 (1979).
- [30] P. M. Richards, Magnetic resonance in superionic conductors, in *Physics of Superionic Conductors*, Topics in Current Physics, Vol. 15, edited by M. B. Salamon (Springer, 1979) Chap. 6, pp. 141–174.
- [31] O. Kanert, Dynamical properties of defects in solids, *Phys. Rep.* **91**, 183 (1982).
- [32] D. Brinkmann, NMR studies of superionic conductors, *Prog. Nucl. Magn. Reson. Spectrosc.* **24**, 527 (1992).
- [33] R. G. Barnes, Nuclear magnetic resonance in metal hydrogen systems, in *Hydrogen in Metals III: Properties and Applications*, edited by H. Wipf (Springer Berlin Heidelberg, Berlin, Heidelberg, 1997) pp. 93–151.
- [34] R. Böhmer, K. R. Jeffrey, and M. Vogel, Solid-state Li NMR with applications to the translational dynamics in ion conductors, *Prog. Nucl. Magn. Reson. Spectrosc.* **50**, 87 (2007).
- [35] A. Kuhn, M. Kunze, P. Sreeraj, H.-D. Wiemhöfer, V. Thangadurai, M. Wilkening, and P. Heitjans, NMR relaxometry as a versatile tool to study Li ion dynamics in potential battery materials, *Solid State Nucl. Magn. Reson.* **42**, 2 (2012).
- [36] J. Habasaki, C. León, and K. L. Ngai, NMR experiments in ionic conductors, in *Dynamics of Glassy, Crystalline and Liquid Ionic Conductors: Experiments, Theories, Simulations* (Springer International Publishing, Cham, 2017) pp. 251–275.
- [37] N. Bloembergen, E. M. Purcell, and R. V. Pound, Relaxation effects in nuclear magnetic resonance absorption, *Phys. Rev.* **73**, 679 (1948).
- [38] M. Villa and J. L. Bjorkstam, Prefactor anomalies, *Solid State Ionics* **9**, 1421 (1983).
- [39] M. T. Chowdhury, R. Takekawa, Y. Iwai, N. Kuwata, and J. Kawamura, Lithium ion diffusion in Li β -alumina single crystals measured by pulsed field gradient NMR spectroscopy, *J. Chem. Phys.* **140**, 124509 (2014).
- [40] J. R. Adelman, D. Fujimoto, M. H. Dehn, S. R. Dunsiger, V. L. Karner, C. D. P. Levy, R. Li, I. McKenzie, R. M. L. McFadden, G. D. Morris, M. R. Pearson, M. Stachura, E. Thoeng, J. O. Ticknor, N. Ohashi, K. M. Kojima, and W. A. MacFarlane, Nuclear magnetic resonance of ^8Li ions implanted in ZnO , *Phys. Rev. B* **106**, 035205 (2022).
- [41] A. Voss, M. R. Pearson, J. Billowes, F. Buchinger, K. H. Chow, J. E. Crawford, M. D. Hossein, R. F. Kiefl, C. D. P. Levy, W. A. MacFarlane, E. Mané, G. D. Morris, T. J. Parolin, H. Saadaoui, Z. Salman, M. Smadella, Q. Song, and D. Wang, *J. Phys. G: Nucl. Part. Phys.* **38**, 075102 (2011).
- [42] W. A. MacFarlane, *Solid State Nucl. Magn. Reson.* **68–69**, 1 (2015).
- [43] A. Bettioli, K. Nugent, and D. Jamieson, The characterisation of high-grade synthetic quartz, corundum and spinel using ionoluminescence (IL), *Nucl. Instrum. Methods Phys. Res., Sect. B* **130**, 734 (1997).
- [44] J. F. Ziegler, M. D. Ziegler, and J. P. Biersack, SRIM – the stopping and range of ions in matter (2010), *Nucl. Instrum. Methods Phys. Res., Sect. B* **268**, 1818 (2010).

- [45] W. MacFarlane, J. Shenton, Z. Salman, A. Chatzichristos, D. Cortie, M. Dehn, D. Fujimoto, V. Karner, R. Kiefl, D. Koumoulis, C. Levy, R. McFadden, I. McKenzie, G. Morris, M. Pearson, M. Stachura, and J. Ticknor, The site and high field β -NMR properties of $^8\text{Li}^+$ implanted in $\alpha\text{-Al}_2\text{O}_3$, *J. Phys.: Conf. Ser.* **2462**, 012009 (2023).
- [46] D. Fujimoto, R. M. L. McFadden, M. H. Dehn, Y. Petel, A. Chatzichristos, L. Hemmingsen, V. L. Karner, R. F. Kiefl, C. D. P. Levy, I. McKenzie, C. A. Michal, G. D. Morris, M. R. Pearson, D. Szunyogh, J. O. Ticknor, M. Stachura, and W. A. MacFarlane, Dynamics of liquid 1-ethyl-3-methylimidazolium acetate measured with implanted-ion ^8Li β -NMR, *Chem. Mater.* **31**, 9346 (2019).
- [47] P. Campone, M. Magliocco, G. Spinolo, and A. Vedda, Ionic transport in crystalline SiO_2 : The role of alkali-metal ions and hydrogen impurities, *Phys. Rev. B* **52**, 15903 (1995).
- [48] A. Ostadhossein, S.-Y. Kim, E. D. Cubuk, Y. Qi, and A. C. T. van Duin, Atomic insight into the lithium storage and diffusion mechanism of $\text{SiO}_2/\text{Al}_2\text{O}_3$ electrodes of lithium ion batteries: ReaxFF reactive force field modeling, *J. Phys. Chem. A* **120**, 2114 (2016).
- [49] J. Plata, J. Breton, and C. Girardet, Theoretical model for the electrodiffusion of M^+ ($M=\text{Li,Na,K}$) ions in a quartz crystal, *Phys. Rev. B* **38**, 3482 (1988).
- [50] P. A. Beckmann, Spectral densities and nuclear spin relaxation in solids, *Phys. Rep.* **171**, 85 (1988).
- [51] C. A. Sholl, Nuclear spin relaxation by translational diffusion in liquids and solids: high- and low-frequency limits, *J. Phys. C: Solid State Phys.* **14**, 447 (1981).
- [52] G. A. Persyn and A. W. Nolle, Low- and high-temperature magnetic resonance and relaxation of NaF:Mn^{2+} , *Phys. Rev.* **140**, A1610 (1965).
- [53] B. C. Thompson and A. W. Nolle, Spin-lattice relaxation in zinc silicofluoride containing manganese and iron, *Phys. Rev.* **180**, 396 (1969).
- [54] M. H. Cohen and F. Reif, Quadrupole effects in nuclear magnetic resonance studies of solids, in *Solid State Physics*, Vol. 5, edited by F. Seitz and D. Turnbull (Academic Press, 1957) pp. 321–438.
- [55] A. V. Nikolaev, N. M. Chchelkatchev, A. V. Bibikov, D. A. Salamatin, and A. V. Tsvyashchenko, Ab initio based description of the unusual increase of the electric field gradient with temperature at Ti sites in rutile TiO_2 , *Phys. Rev. B* **102**, 174305 (2020).
- [56] A. Sartbaeva, S. A. Wells, S. A. T. Redfern, R. W. Hinton, and S. J. B. Reed, Ionic diffusion in quartz studied by transport measurements, SIMS and atomistic simulations, *J. Phys.: Condens. Matter* **17**, 1099 (2005).
- [57] M. G. Jani, L. E. Halliburton, and A. Halperin, Observation of a simple lithium-associated electron trap in crystalline SiO_2 , *Phys. Rev. Lett.* **56**, 1392 (1986).
- [58] T. M. Wilson, J. A. Weil, and P. S. Rao, Electronic structure of the interstitial lithium-associated electron trap in crystalline quartz, *Phys. Rev. B* **34**, 6053 (1986).
- [59] U. Wahl, Emission channeling studies of Li in semiconductors, *Phys. Rep.* **280**, 145 (1997).
- [60] F. Cora and C. Pisani, A quantum-mechanical ab initio simulation of neutral and charged point defects in alpha-quartz, *Modell. Simul. Mater. Sci. Eng.* **2**, 965 (1994).
- [61] A. Sartbaeva, S. A. Wells, and S. A. T. Redfern, Li^+ ion motion in quartz and β -eucryptite studied by dielectric spectroscopy and atomistic simulations, *J. Phys.: Condens. Matter* **16**, 8173 (2004).
- [62] N. Varini, D. Ceresoli, L. Martin-Samos, I. Girotto, and C. Cavazzoni, Enhancement of DFT-calculations at petascale: Nuclear Magnetic Resonance, hybrid density functional theory and Car-Parrinello calculations, *Comput. Phys. Commun.* **184**, 1827 (2013).
- [63] C. J. Pickard and F. Mauri, All-electron magnetic response with pseudopotentials: NMR chemical shifts, *Phys. Rev. B* **63**, 245101 (2001).
- [64] M. Profeta, F. Mauri, and C. J. Pickard, Accurate first principles prediction of ^{17}O NMR parameters in SiO_2 : Assignment of the zeolite ferrierite spectrum, *J. Am. Chem. Soc.* **125**, 541 (2003).
- [65] D. R. Spearing, I. Farnan, and J. F. Stebbins, Dynamics of the α - β phase transitions in quartz and cristobalite as observed by in-situ high temperature ^{29}Si and ^{17}O NMR, *Phys. Chem. Miner.* **19**, 307 (1992).
- [66] J. Valenzuela Reina, F. Civaia, A. F. Harper, C. Scheurer, and S. S. Köcher, The EFG rosetta stone: translating between DFT calculations and solid state NMR experiments, *Faraday Discuss.* **255**, 266 (2025).
- [67] A. N. Trukhin, Excitons in SiO_2 : a review, *J. Non-Cryst. Solids* **149**, 32 (1992).
- [68] The biexponential is unrelated to the common circumstance in solid state NMR where only one quadrupole satellite can be irradiated by an RF pulse. Here, the SLR measurements use no RF, and the initial spin state has very pure dipolar polarization from the optical pumping. Nor is it due to slow quadrupolar fluctuations[101], which give rise at most to a very small fast component (of a few %).
- [69] M. Hossain, H. Saadaoui, T. Parolin, Q. Song, D. Wang, M. Smadella, K. Chow, M. Egilmez, I. Fan, R. Kiefl, S. Kreitzman, C. Levy, G. Morris, M. Pearson, Z. Salman, and W. MacFarlane, The spin lattice relaxation of ^8Li in simple metals, *Physica B* **404**, 914 (2009).
- [70] B. Hitti, S. R. Kreitzman, T. L. Estle, E. S. Bates, M. R. Dawdy, T. L. Head, and R. L. Lichti, Dynamics of negative muonium in n-type silicon, *Phys. Rev. B* **59**, 4918 (1999).
- [71] B. B. Baker, Y. G. Celebi, R. L. Lichti, P. W. Mengyan, and E. Catak, Motional characteristics of positively charged muonium defects in In_2O_3 , *AIP Conf. Proc.* **1583**, 323 (2014).
- [72] O. Hartmann, E. Karlsson, E. Wäckelgård, R. Wäppling, D. Richter, R. Hempelmann, and T. O. Niinikoski, Diffusion and trapping of muons in aluminum: New experiments and comparison with Kondo theory, *Phys. Rev. B* **37**, 4425 (1988).
- [73] M. C. Jollands, M. Blanchard, and E. Balan, Structure and theoretical infrared spectra of OH defects in quartz, *Eur. J. Mineral.* **32**, 311 (2020).
- [74] S. Devautour-Vinot, O. Cambon, N. Prud'homme, J. C. Giuntini, J.-J. Boy, and G. Cibiel, Complex impedance spectroscopy of alkali impurities in as-grown, irradiated and annealed quartz, *J. Appl. Phys.* **102**, 104102 (2007).
- [75] A. Halperin, M. G. Jani, and L. E. Halliburton, Correlated ESR and thermoluminescence study of the $[\text{SiO}_4/\text{Li}]^0$ center in quartz, *Phys. Rev. B* **34**, 5702 (1986).
- [76] J. H. Brewer, Muonium in quartz, *Hyperfine Interact.* **8**, 375 (1981).
- [77] J. H. Brewer, G. D. Morris, D. J. Arseneau, D. G. Eshchenko, V. G. Storchak, and J. Bermejo, Delayed muonium formation in quartz, *Physica B* **289-290**, 425 (2000).
- [78] A. Stoneham, Electronic and defect processes in oxides. the polaron in action, *IEEE Trans. Dielectr. Electr. Insul.* **4**, 604 (1997).
- [79] J. B. Varley, A. Janotti, C. Franchini, and C. G. Van de Walle, Role of self-trapping in luminescence and p -type conductivity of wide-band-gap oxides, *Phys. Rev. B* **85**, 081109 (2012).
- [80] D. L. Griscom, Trapped-electron centers in pure and doped glassy silica: A review and synthesis, *J. Non-Cryst. Solids* **357**,

- 1945 (2011).
- [81] A.-M. El-Sayed, M. B. Watkins, V. V. Afanas'ev, and A. L. Shluger, Nature of intrinsic and extrinsic electron trapping in SiO₂, *Phys. Rev. B* **89**, 125201 (2014).
- [82] J. M. Costantini, F. Brisard, G. Biotteau, E. Balanzat, and B. Gervais, Self-trapped exciton luminescence induced in alpha quartz by swift heavy ion irradiations, *J. Appl. Phys.* **88**, 1339 (2000).
- [83] F. Preusser, M. L. Chithambo, T. Götte, M. Martini, K. Ramseyer, E. J. Sendezer, G. J. Susino, and A. G. Wintle, Quartz as a natural luminescence dosimeter, *Earth Sci. Rev.* **97**, 184 (2009).
- [84] R. A. Weeks and M. Abraham, Electron spin resonance of irradiated quartz: Atomic hydrogen, *J. Chem. Phys.* **42**, 68 (1965).
- [85] D. L. Griscom, Defect structure of glasses: Some outstanding questions in regard to vitreous silica, *J. Non-Cryst. Solids* **73**, 51 (1985), see section 3.2.
- [86] M. Martini, F. Meinardi, and A. Vedda, The role of alkali ions in the 190 K TSL peak in quartz, *Radiat. Meas.* **32**, 673 (2000).
- [87] M. Martini, M. Fasoli, A. Galli, I. Villa, and P. Guibert, Radioluminescence of synthetic quartz related to alkali ions, *J. Lumin.* **132**, 1030 (2012).
- [88] W. Hayes, M. J. Kane, O. Salminen, R. L. Wood, and S. P. Doherty, ODMR of recombination centres in crystalline quartz, *J. Phys. C: Solid State Phys.* **17**, 2943 (1984).
- [89] S. Ismail-Beigi and S. G. Louie, Self-trapped excitons in silicon dioxide: Mechanism and properties, *Phys. Rev. Lett.* **95**, 156401 (2005).
- [90] W. A. MacFarlane, T. J. Parolin, D. L. Cortie, K. H. Chow, M. D. Hossain, R. F. Kiefl, C. D. P. Levy, R. M. L. McFadden, G. D. Morris, M. R. Pearson, H. Saadaoui, Z. Salman, Q. Song, and D. Wang, ⁸Li⁺ β -NMR in the cubic insulator MgO, *J. Phys.: Conf. Ser.* **551**, 012033 (2014).
- [91] G. Will, M. Bellotto, W. Parrish, and M. Hart, Crystal structures of quartz and magnesium germanate by profile analysis of synchrotron-radiation high-resolution powder data, *J. Appl. Crystallogr.* **21**, 182 (1988).
- [92] P. Giannozzi *et al.*, Quantum ESPRESSO toward the exascale, *J. Chem. Phys.* **152**, 154105 (2020).
- [93] P. Giannozzi *et al.*, Advanced capabilities for materials modelling with QUANTUM ESPRESSO, *J. Phys.: Condens. Matter* **29**, 465901 (2017).
- [94] P. Giannozzi *et al.*, QUANTUM ESPRESSO: a modular and open-source software project for quantum simulations of materials, *J. Phys.: Condens. Matter* **21**, 395502 (2009).
- [95] N. Troullier and J. L. Martins, Efficient pseudopotentials for plane-wave calculations, *Phys. Rev. B* **43**, 1993 (1991).
- [96] C. Tantardini, A. G. Kvashnin, and D. Ceresoli, GIPAW pseudopotentials of *d* elements for solid-state NMR, *Materials* **15**, 3347 (2022).
- [97] P. Bonfà, F. Sartori, and R. De Renzi, Efficient and reliable strategy for identifying muon sites based on the double adiabatic approximation, *J. Phys. Chem. C* **119**, 4278 (2015).
- [98] H. J. Monkhorst and J. D. Pack, Special points for brillouin-zone integrations, *Phys. Rev. B* **13**, 5188 (1976).
- [99] B. Movaghar, G. W. Sauer, and D. Würtz, Time decay of excitations in the one-dimensional trapping problem, *J. Stat. Phys.* **27**, 473 (1982).
- [100] D. Herlach, Investigation of defects and muon diffusion in metals by positive muon spin rotation, in *Recent Developments in Condensed Matter Physics*, Vol. 1, edited by J. T. Devreese, L. F. Lemmens, V. E. Van Doren, and J. Van Royen, European Physical Society Condensed Matter Division (Plenum, New York, NY, 1981) pp. 93–110.
- [101] K. D. Becker, Nuclear magnetic relaxation induced by the dynamics of lattice defects in solids ($I = 3/2$, $I = 2$, $I = 5/2$), *Z. Naturforsch. A* **37**, 697 (1982).